

CubeSats Reach the Millisecond X-Ray Domain: Crab Pulsar Timing with *SpIRIT/HERMES*

WLADIMIRO LEONE ^{1,2,3} R. MEARNs ⁴ T. DI SALVO ² L. BURDERI ^{5,6} M. THOMAS ⁴ M. TRENTI ⁴
F. FIORE ³ E. J. MARCHESINI ⁷ R. CAMPANA ^{7,8} G. BARONI ³ M. DAFČÍKOVÁ ^{3,9} A. ANITRA ²
Y. EVANGELISTA ¹⁰ A. SANNA ⁵ S. PUCCETTI ¹¹ R. IARIA ² S. BARRACLOUGH ⁴ M. ORTIZ DEL CASTILLO ⁴
R. BERTACIN ¹¹ P. BELLUTTI ^{12,13} G. BERTUCCIO ^{14,15} A. CHAPMAN ¹⁶ G. CABRAS ⁵ F. CERAUDO ¹⁰
T. CHEN ¹⁷ M. CITOSI ³ R. CRUPI ¹⁸ G. DELLA CASA ¹⁰ E. DEMENEV ¹³ G. DILILLO ^{19,11} M. FEROCI ¹⁰
F. FICORELLA ¹³ M. FIORINI ²⁰ N. GAO ¹⁷ A. GUZMAN ²¹ P. HEDDERMAN ²¹ A. HUDRAP ²² C. LABANTI ⁷
G. LA ROSA ⁶ P. MALCOVATI ²³ J. MCROBBIE ⁴ F. MELE ^{14,24,10} G. MOLERA CALVÉS ²⁵ J. MORGAN ⁴
G. MORGANTE ⁷ B. NEGRI ¹¹ D. NOVEL ¹³ P. NOGARA ⁶ A. NUTI ¹⁰ E. O'BRIEN ⁴ G. PEPPONI ¹³
M. PERRI ²⁶ A. PICCIOTTO ¹³ R. PIAZZOLLA ¹¹ S. PIRROTTA ¹¹ S. PLIEGO CABALLERO ²¹ A. RACHEVSKI ²⁷
I. RASHEVSKAYA ²⁷ A. RIGGIO ⁵ F. RUSSO ⁶ A. SANTANGELO ²¹ G. SOTTILE ⁶ C. TENZER ²¹ Y. TAO ⁴
S. TREVISAN ¹ A. VACCHI ¹⁸ G. ZAMPA ²⁷ N. ZAMPA ^{18,27} S. XIONG ¹⁷ S. YI ¹⁷ A. WOODS ⁴ S. ZHANG ¹⁷ AND
N. ZORZI ¹³

¹University of Trento, Department of Physics, Via Sommarive, 14, 38123 Povo TN, Italy

²University of Palermo, Dipartimento di Fisica e Chimica "E. Segrè", Via Archirafi subcampus., Via Archirafi, 36, 90123 Palermo, Italy

³INAF/Osservatorio Astronomico di Trieste, via G. Tiepolo 11, I-34124 Trieste, Italy

⁴School of Physics, The University of Melbourne, VIC 3010, Australia

⁵Dipartimento di Fisica, Università degli Studi di Cagliari, SP Monserrato-Sestu, km 0.7, I-09042 Monserrato, Italy

⁶INAF/IASF Palermo, via Ugo La Malfa 153, I-90146 Palermo, Italy

⁷INAF/OAS, Via Piero Gobetti, 93/3, 40129 Bologna, Italy

⁸INFN Sezione di Bologna, Viale Berti Pichat 6/2, 40127 Bologna, Italy

⁹Department of Theoretical Physics and Astrophysics, Masaryk University, Kotlářská 267/2, 611 37 Brno, Czech Republic

¹⁰INAF/IAPS, Via del Fosso del Cavaliere, 100, 00133 Roma, Italy

¹¹ASI - Italian Space Agency, Via del Politecnico snc, 00133, Rome, Italy

¹²INAF/OAB, via E. Bianchi 46 I-23807 Merate, Italy

¹³Fondazione Bruno Kessler - Sensors and Devices, Via Sommarive, 18, 38123 Povo TN, Italy

¹⁴Politecnico di Milano, Dept. Electronics, Information and Bioengineering, Via Giuseppe Ponzio, 34, 20133 Milano MI

¹⁵INFN Milano, Via Giovanni Celoria, 16, 20133 Milan, Italy

¹⁶Department of Mechanical Engineering, University of Melbourne, VIC 3010, Australia

¹⁷IHEP/CAS, 19B Yuquan Road, Shijingshan District, Beijing, China, 100049

¹⁸Department of Mathematics, Computer Science and Physics, University of Udine, via delle Scienze, 206, 33100 Udine, Italy

¹⁹INAF, Osservatorio Astronomico di Roma, Via Frascati 33, Monte Porzio Catone, Roma, 00040, Italy

²⁰INAF/IASF Milano, Via Alfonso Corti 12, I-20133 Milano, Italy

²¹Institut für Astronomie und Astrophysik, Sand 1, 72076 Tübingen, Germany

²²Skylabs

²³University of Pavia, Dipartimento di Ingegneria Industriale e dell'Informazione, Via Adolfo Ferrata 5, 27100 Pavia

²⁴INFN Milano, Via Giovanni Celoria, 16, 20133 Milan, Italy

²⁵Department of Physics, University of Tasmania, Clark Road, Hobart TAS 7005, Australia

²⁶INAF/OAR, Via Frascati 33, I-00040, Monte Porzio Catone, Italy

²⁷INFN Trieste, Padriciano, 99, 34149 Trieste, Italy

ABSTRACT

The *High Energy Rapid Modular Ensemble of Satellites (HERMES)* instrument is a compact X/ γ -ray spectrometer operating on board the 6U (11 kg) *SpIRIT* CubeSat. The payload is particularly well suited for the observation of cosmic transients such as Gamma-Ray Bursts and bright pulsars thanks to its unique broadband sensitivity from a few keV to a few MeV and the temporal resolution down to half a microsecond. We report here the detection of the ~ 33 ms Crab pulsar double-peaked pulse profile obtained by considering the canonical Crab ephemerides as provided by the Jodrell Bank catalog. We collected approximately $5.7 \cdot 10^4$ photons from 730 s of observations, in the 3 keV – 2 MeV energy band, during a single operation, and achieved a 5σ pulse profile significance in the 3–11.5

keV energy band with binning at the ms scale. The results demonstrate that *SpIRIT/HERMES* can achieve millisecond timing accuracy at high energies and, thanks to its wide field of view and broad energy band, has the potential to contribute to GRB monitoring in the near future. Such capabilities were previously the domain of flagship observatories, underscoring the performance of the *HERMES* instrument with its compact form factor.

Keywords: High Energy astrophysics (739) – Pulsar timing method (1305) – Spectrometers (1554)

1. INTRODUCTION

High-energy astrophysics in the X-ray and γ -ray bands has traditionally been driven by large space-borne observatories, whose substantial collecting area, stable pointing, and precise timing have enabled detailed studies of compact objects and fast variability. Missions such as *RXTE*, *NuSTAR*, and *NICER* have established the current state of the art in sensitivity and absolute timing, providing key insights into pulsars, accreting systems, and high-energy transients (J. H. Swank 1999; M. van der Klis 2006; K. K. Madsen et al. 2015; M. Vivekanand 2021). In recent years, advances in detector technology and onboard electronics have enabled CubeSat-class missions to access the X-ray and γ -ray sky with compact detectors and increasing scientific maturity, particularly in the context of time-domain and transient astrophysics (T. Tamagawa et al. 2025; A. Pál et al. 2023).

The *High Energy Rapid Modular Ensemble of Satellites (HERMES)* payload is an innovative and compact (~ 1 U, i.e. $10 \times 10 \times 10$ cm³ volume, with ≈ 1.6 kg mass) X/ γ -ray spectrometer operating in orbit onboard the 6U *SpIRIT (Space Industry – Responsive – Intelligent – Thermal nanosatellite)* CubeSat (M. Trenti et al. 2024). The payload adopts, for the first time in space, a siswich (*silicon sandwich*) architecture, in which Silicon Drift Detectors (SDDs) are used to both detect (i) directly cosmic X-rays and (ii) gamma-rays via optical photons produced by gamma-rays scintillation in GAGG:Ce crystals (Y. Evangelista et al. 2020a,b, 2024). The provides a unique broadband sensitivity from a few keVs to a few MeVs. A second key feature of the *HERMES* payload is its exquisite event timing. While the siswich configuration enables fast event-by-event readout, the sub-microsecond performance is primarily set by the back-end time-tagging chain. The resulting time resolution is ~ 0.5 μ s, about 5–7 times better than that of previous instruments dedicated to this task (R. Campana et al. 2022; G. Dilillo et al. 2024).

The instrument has been developed as the core element of the *HERMES (+ SpIRIT) Pathfinder*, an in-orbit demonstration mission consisting of a constellation of six 3U and one 6U CubeSats (F. Fiore et al. 2020, 2025), each equipped with an identical payload (Y. Evangelista et al. 2020b). The Pathfinder aims to detect and contribute to the localization high-energy astrophysical transients, such as γ -ray bursts (GRBs), with high timing precision, broad sky coverage, and good sensitivity in terms of detection threshold photon flux (at 1 s for long and 64 ms for short GRBs) in the 50–300 keV band: 0.8 ph cm⁻² s⁻¹ for long GRBs and 5.6 ph cm⁻² s⁻¹ for short GRBs (G. Ghirlanda et al. 2024). The mission architecture leverages a distributed and modular approach to improve responsiveness and localization accuracy through inter-satellite temporal triangulation techniques (K. Hurley et al. 2013; F. Fiore et al. 2021; M. Thomas et al. 2023; W. Leone et al. 2025).

This paper presents the first timing analysis of Crab pulsar data obtained with the *HERMES* payload on board *SpIRIT*. The Crab is a composite system consisting of a young pulsar (PSR B0531+21) and a surrounding synchrotron nebula, and is one of the most widely used calibration sources in high-energy astrophysics. Both the pulsar and the nebula emit across the entire electromagnetic spectrum. Because of its high and stable flux, especially in the X-ray and γ -ray bands, the Crab is considered a “standard candle” for instrument verification (M. G. Kirsch et al. 2005). Furthermore, the Crab pulsation, characterized by its well-known double-peaked profile with a period of about 33 ms, is used to evaluate the timing accuracy of many instruments (A. H. Rots et al. 2004). In this work we present the detection of the Crab pulsar profile with *HERMES*. Independently, a similar result was recently obtained by another CubeSat mission, *Ninjasat*, using an X-ray gas detector sensitive in the 2–50 keV band (T. Tamagawa et al. 2025). This result was achieved with an exposure of 11 ks and thanks to a collimator that narrows the field of view (FoV) to $\approx 2.1^\circ$, thereby substantially reducing the non-pulsed contribution from the cosmic X-ray background. Both results demonstrate that a CubeSat-class, low-cost mission can deliver timing performance previously achievable only with larger, dedicated observatories, marking a step toward precision time-domain astrophysics from nanosatellites.

This paper is organized as follows. Section 2 summarizes *SpIRIT/HERMES* characteristic and science operations. Section 3 explores the Crab Pulsar timing analysis, and the Pulse Profile determination with the *SpIRIT/HERMES*

non-collimated detector using a 730s total exposure. Section 4 illustrates the comparison of the *SpIRIT/HERMES* timing capabilities with the *NuSTAR* and *NICER* observatories and validate the detected *SpIRIT/HERMES* Pulse profile by modeling it with the *NuSTAR* profile.

Finally, the Appendix demonstrates analytically and via Monte Carlo tests that the relatively short exposure time considered in this analysis is expected to lead to the significant Crab detection with *SpIRIT/HERMES* inferred from the observations.

2. *SpIRIT/HERMES*

The first *HERMES* payload has been launched and operated in space thanks to international cooperation between Australia and Italy. In this section we present an overview of the *SpIRIT* mission and of the early in-orbit operations of *HERMES*.

2.1. *The SpIRIT satellite*

The *SpIRIT* satellite is a 6U-XL nanosatellite, launched into a Sun-Synchronous orbit on 1st December 2023 (M. Trenti et al. 2024). It has been successfully and continuously operating for over 2 years in orbit at the time of writing. Australian Space Agency funded elements include the spacecraft platform, supplied by an Australian commercial provider, an instrument control unit, i.e., the Payload Management System (PMS) (M. O. del Castillo et al. 2025), a thermal control unit (TheMIS; M. Ortiz del Castillo et al. 2024a), an Iridium and GPS payload (R. Mearns et al. 2024) and a Graphic Processing Unit and multi-camera system (M. Ortiz del Castillo et al. 2024b), all developed by the University of Melbourne. The *HERMES* payload and the S-band module have been supplied by the Italian Space Agency through a cooperative agreement with the University of Melbourne.

2.2. *The HERMES payload*

Each *HERMES* detector comprises 60 Cerium-doped Gadolinium-Aluminium-Gallium garnet (GAGG:Ce) inorganic scintillator crystals (with a cross-sectional area of $6.94 \times 12.1 \text{ mm}^2$ and a thickness of 15 mm) coupled to 12 arrays of 2×5 SDDs (Y. Evangelista et al. 2020b; R. Campana et al. 2022) cells, each with a 25 mm^2 sensitive area, segmented into four independent quadrants of 30 SDD cells each. Thanks to their sensitivity to both X-ray and optical photons, SDDs provide a dual readout channel: they detect low-energy X-rays directly in the silicon (*X-mode*) and, when coupled to a scintillator, they also detect γ -rays indirectly by collecting the optical scintillation light produced in the crystal (*S-mode*). In the baseline layout, each crystal is optically coupled to two SDD cells, so that the resulting light-sharing pattern enables a reliable discrimination between X- and S-events (R. Campana et al. 2024). This so-called “siswich” architecture offers wide spectral sensitivity, spanning a few keV to several MeV, and exceptional time resolution, reaching sub-microsecond precision, thanks to the fast response of GAGG:Ce crystals and the fine segmentation of the SDD mosaics (R. Campana et al. 2024). An on-board chip-scale atomic clock provides an extremely stable 10 MHz clock (that can be synchronized with the GPS Pulse Per Second signal) for the accurate time tagging of the events (R. Campana et al. 2024). The SDD signals are readout by the Application Specific Integrated Circuit (ASIC), called LYRA (M. Gandola et al. 2021), a multi-chip architecture of 120 Front-End chips (LYRA-FE), placed in close proximity to the SDD anodes, and four 32-channel Back-End chips (LYRA-BE), using an innovative current-mode transmission strategy which minimizes interchannel crosstalk while keeping a low-noise performance and a low ($<1 \text{ mW/ch}$) power consumption. The payload field of view is energy-dependent: it is $\sim 3 \text{ sr}$ in the 3–20 keV band and broadens at higher energies as the shielding becomes less effective, reaching $\sim 5 \text{ sr}$ above 50 keV (R. Campana et al. 2020; G. Ghirlanda et al. 2024).

The payload on *SpIRIT* achieved first light in February 2024. Since then, it has been operated as part of the satellite commissioning phase and to achieve orbital calibration (G. Baroni et al. 2024). Unfortunately, prior to delivery of the payload to the University of Melbourne for integration, one of the four *HERMES* quadrants was damaged, and thus has not been operational after the payload integration on the spacecraft. This results in an overall reduction of about 25% in effective area (with an associated sensitivity reduction of $\sqrt{0.75}$), which is accounted for in the analysis presented in this paper.

During Crab pulsar observations, the nominal low-energy threshold for each active channel ranges from 3 to 7 keV, due to variations in the channel-to-channel process and the working principle of the discrimination circuit (Y. Evangelista et al. 2020b). Accordingly, throughout this paper, we adopt 3 keV as the minimum energy of the *HERMES* effective area to ensure that any potential source photons are included in the analysis.

2.3. SpIRIT operations

As *SpIRIT* represents the first satellite launched by the University of Melbourne and by the commercial platform provider, as well as the first flight of the *HERMES* payload, a protracted commissioning period has transpired, with a number of operational limitations and anomalies accruing over the operating lifetime. These limitations and anomalies have had an impact on the execution and design of *HERMES* observational operations, and so they are briefly outlined here.

- The spacecraft platform provides a scripting engine to organize and schedule custom operations, however these scripts are limited to a critical maximum memory size ¹, which introduces significant challenges in scheduling complex operations such as those associated with a scientific instrument.
- The PMS instrument control unit provides an interface between all *SpIRIT* payloads, including the *HERMES* instrument, and the spacecraft platform, granting on-board data storage, power management, and a commanding interface via the platform scripting engine allowing flexible operations. The *HERMES* instrument is preferentially supplied with an uninterruptible power supply by the PMS to forestall any power supply issues (M. O. del Castillo et al. 2025). Unfortunately, following deployment of the second solar panel in July 2024, the PMS has been suffering from randomly occurring resets, at a rate of approximately 6 resets/hr. While a direct root cause of these resets has not been identified to date, there appears to be a strong geographic correlation, which interestingly excludes regions of high-radiation such as the South Atlantic Anomaly (Ortiz del Castillo et al., in prep). These PMS anomalies have directly affected the operational cadence of the *HERMES* instrument, with early commissioning operations, such as this observation of the Crab Pulsar/Nebula, directly terminated by any single reset.
- Since launch, *SpIRIT* has been affected by a number of limitations of the Attitude and Determination Control system (ADCS). Primarily, *SpIRIT* has a strong intrinsic magnetic dipole of the order of 0.6Am^2 (Wen et al. under review). When this field interacts with the Earth’s field, a significant torque can be induced on the spacecraft. Consequently, the spacecraft reaction wheels must rapidly increase speed to compensate for this induced torque. Once the safety threshold of the wheels is exceeded, the spacecraft must enter a ”detumbling” period in which the wheels are slowed, the spacecraft tumbles, and the angular momentum is slowly bled out of the spacecraft using magnetorquers. Due to the strength of the *SpIRIT* intrinsic magnetic field, a detumbling period can occur as frequently as every orbit if *SpIRIT* maintains a static attitude for an extended period. Critically, in order to achieve an acceptable level of attitude determination and control during eclipse, *SpIRIT* star-tracker must be pointed as close to Zenith as possible. However, fixing both the *HERMES* instrument bore-sight, and the star-tracker bore-sight (orthogonal vectors), for an extended period, results in an attitude most susceptible to the momentum build-up effect of the intrinsic dipole. This anomaly, therefore, further limits the possible operational cadence of the *HERMES* instrument while observing a particular astrophysical source.
- Due to both the ADCS and PMS anomalies, the commissioning of the payload GPS timing source was not possible prior to this observation. Consequently, absolute timing information is provided to the payload by means of a “mock” GPS signal. This mock signal is synchronized to the platform’s GPS clock with uncertainty of up to 1 s (the mock signal synchronization is rounded down to the nearest second) and provided to the *HERMES* instrument once a second. Because following a PMS reset anomaly the *HERMES* payload goes through a safe shutdown sequence, its internal atomic clock is turned off. Therefore, high timing precision for photon arrival time is limited to a single uninterrupted operation with *HERMES* (i.e., consistent tracking/phase connection between observing segments in time is not ensured through the power cycling boundary).
- *SpIRIT* carries an S-Band radio for payload data downlink that was planned for use through the *HERMES* TP/SP ground segment. However, the link had not been commissioned at the time of these observations. Therefore, all payload data that are part of this paper were downlinked via the Telemetry & TeleCommand link provided by the UHF radio. This limits the overall transmission rate of payload data to about 200 kB/day after accounting for higher priority spacecraft health telemetry. Consequently, the planning, execution, data retrieval, and analysis iterative loop during commissioning activities was protracted. In fact, considering the time needed for uplink of telecommands, typically one iterative set of experiments could be done on a timescale of one week.

¹ The actual value is proprietary commercial information of the platform provider and experience in orbit has shown variability depending on other processes running on board.

- Due to risk aversion to exposing the *HERMES* instrument to direct Sunlight during operations in case of loss of attitude control, *HERMES* operations at the time of data acquisition were limited to eclipse periods.

We note that the presence of anomalies and in-orbit limitations compared to pre-flight nominal configuration is typical for CubeSat missions, in particular for first flights. This is exemplified by the historical failure rate of CubeSats, with about 40% probability of infant mortality for University-led CubeSats (“dead on arrival” or loss of contact within 30 days post launch²). Therefore, by this metric, the operations for two years of a complex multi-organisation CubeSat such as *SpIRIT* with both technology demonstration of payloads in orbit and scientific data acquisition — albeit with challenges — represent a successful outcome.

2.4. HERMES observations of Crab

The design of the observation of the Crab Pulsar with the *SpIRIT* nanosatellite is a complex multi-constraint optimisation problem; the instrument has to be operated in regions of low background radiation between the radiation belts (the contours pictured in the top left panel of Figure 1), but also in eclipse. Further, the Crab Pulsar should be located as close to the spacecraft zenith (i.e., the centre of the *HERMES* field of view) as possible during the observation, to maximise the effective collecting area of photons. Competing with these constraints, however, are those to ensure the reliable operation of the platform throughout the observation. To minimise the chance of anomalous PMS resets, the observation should occur in those geographic regions with a recorded low-likelihood of resets (primarily the Indian and Atlantic oceans). Additionally, to ensure a continuous attitude solution (and thereby ensure that the Crab Pulsar remains stable in the *HERMES* field of view), *SpIRIT* star-tracker should point as close to Zenith as possible.

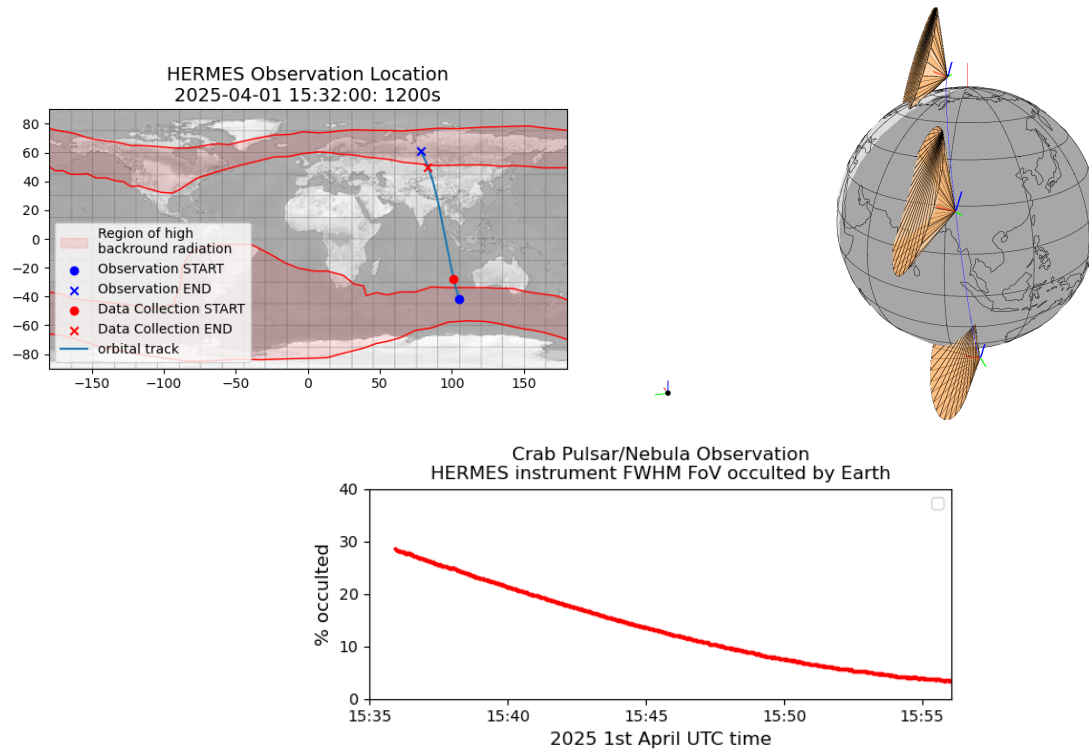


Figure 1. *SpIRIT* and *HERMES* instrument FoV configuration during the Crab Pulsar/Nebula observation reported here. **Top left:** Orbital track of *SpIRIT* during data collection, with high background regions shown as shaded red, data collection began at 2025-04-01 15:36:06 UTC, and ended at 2025-04-01 15:56:06 UTC. **Top right:** Three-dimensional display of *SpIRIT* location, and *HERMES* instrument FoV, during the operation. **Bottom:** *HERMES* FoV occultation by Earth during the observation (for background noise estimation).

² <https://digitalcommons.usu.edu/cgi/viewcontent.cgi?article=3415&context=smallsat>

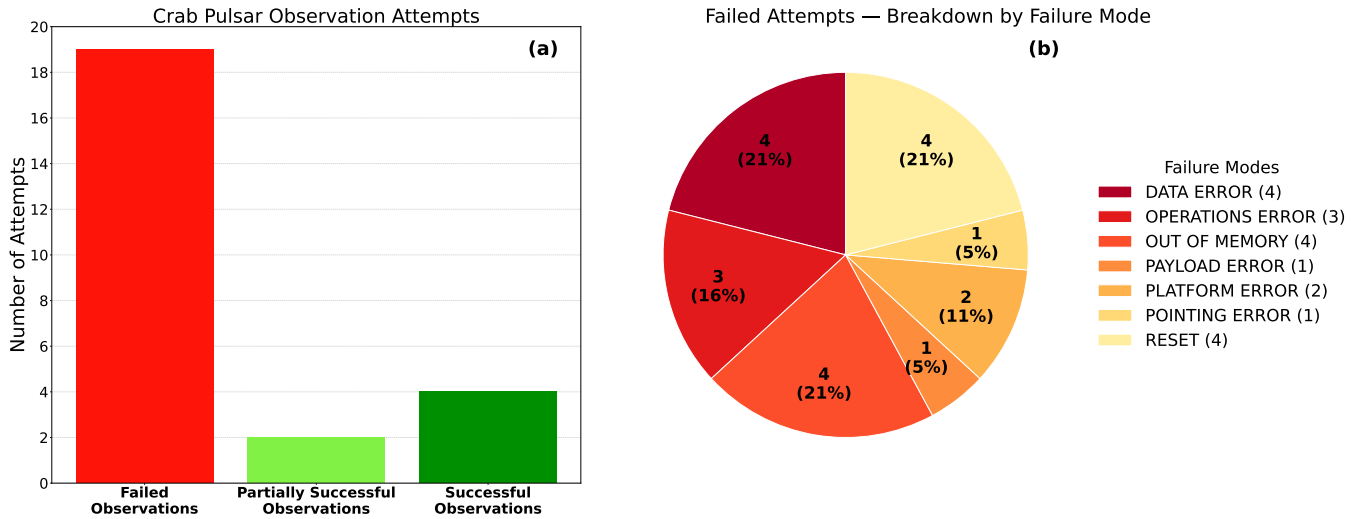


Figure 2. (a) Observation success statistics for the *SpIRIT* Crab Pulsar/Nebula observing campaign from 2024 December 11 to 2025 April 1. (b) Breakdown of the failed observation attempts by failure category.

Given these constraints the observational campaign of the Crab Pulsar/Nebula began in mid December 2024, with 25 observation attempts made over the following months to refine the process, mitigate errors within *HERMES*, the payload suite, and the platform, and yield a sufficiently long dataset for the extraction of a pulsed signal. Figure 2 details the outcome of all observational attempts throughout this campaign. While only the primary failure mode of each observation attempt is listed, additional faults may have occurred. Of particular note as secondary failure mode is the lack of a sufficient attitude control for the duration of the observations. A brief description of each of the operation success status classifications is as follows:

- **Observation Attempt Failure Mode:**

- **DATA ERROR:** Due to a design limitation of the instrument flight software in the (early) version delivered for *SpIRIT*, more than 30% of data files over a size threshold could not be offloaded from the *HERMES* instrument.
- **OPERATIONS ERROR:** Resources were not made available to the platform due to mission operations centre errors.
- **OUT OF MEMORY:** The operational scripts for telecommanding the observation exceeded the on-board memory limitations (this typically occurs as modifications to the operational script are rolled out to the spacecraft for the first time in order to mitigate other systematic problems).
- **PAYLOAD ERROR:** The *HERMES* instrument failed to respond to a request within the timeout, and the observation was terminated.
- **PLATFORM ERROR:** The observation was not run due to an onboard corruption of the schedule file or other recoverable platform software/hardware issues.
- **POINTING ERROR:** No other fault was experienced, but the spacecraft ADCS was unable to maintain an attitude lock on the Crab Pulsar/Nebula sufficient to meet the scientific observation requirements.
- **RESET:** An anomalous PMS reset was experienced, terminating the *HERMES* observation.

- **Partially Successful Observations:** Similar to the aforementioned DATA ERROR classification, but in this case more than 70% of data files could be offloaded from the *HERMES* instrument.
- **Successful Observations:** No faults occurred during the operation, and a sufficient fraction of data files could be offloaded from the *HERMES* instrument.

Most failed observations were scheduled as single ~ 40 s exposures. Successful detections of the Crab were obtained in three separate ~ 40 s exposures and in longer integrations of ~ 250 s, ~ 400 s, and ~ 700 s, the latter being analyzed in this work. Considering the total attempted exposure time, the overall observing efficiency was approximately 50%.

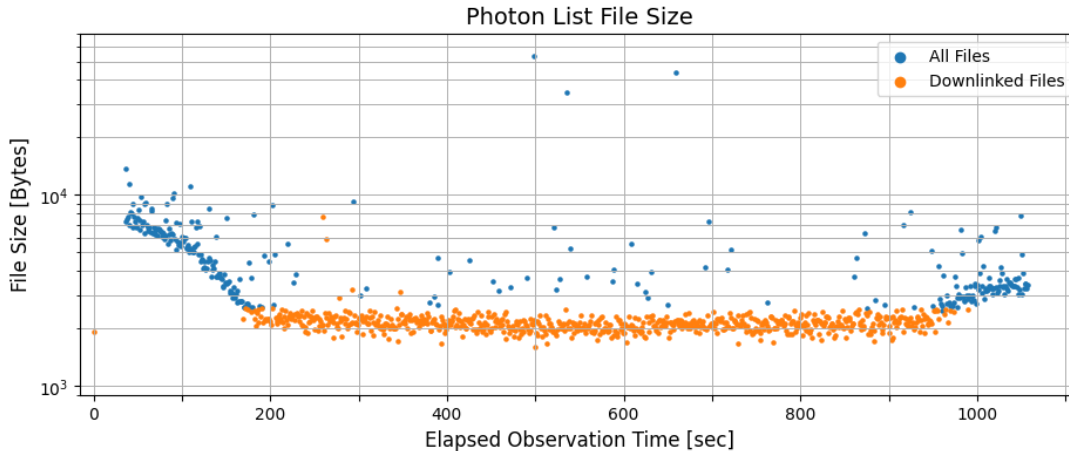


Figure 3. CALibration mode file-sizes vs. elapsed observation time. Only the files in orange were downlinked from the spacecraft, forming the non-contiguous 730 s observation dataset.

The last observation of the campaign was executed on 2025-04-01, 15:32 UTC and the instrument observed for a total of 1200 s. The orbital track of this operation is detailed in Figure 1, along with a visual representation of the HERMES instrument pointing along the orbit, and an estimate of the HERMES FoV occulted by Earth. During the observing window, the ADCS system reported that the HERMES instrument was centered within 1° of (RA, DEC) = ($5^h34.53^m$, 22.01°) (the Crab coordinates). As a caveat, we note that the accuracy and the repeatability of the ADCS has not been independently validated. Therefore, a conservative offset of 10° from zenith has been considered on all attitude estimates. However, an offset of this magnitude has limited impact on the observations described, as the sensitivity of the instrument decreases with $\cos\theta$ of the offset angle for a source at zenith.

When correctly configured, the *HERMES* instrument produces a single data file per second, timestamped according to the *mock* GPS signal described above, thus the 1200 s 2025-04-01 Crab Pulsar/Nebula observation produced 1200 data files on the HERMES instrument. At the time of the observations, the on-board file processing operations were still undergoing commissioning activities. Consequently, the on-board operation to query the size of all data files required ~ 2 hours of computing time. Several attempts were needed to overcome the occurrence of PMS resets. Ultimately, an sufficiently complete list of 1023/1200 data files was produced. Figure 3 shows output of the operation, with the size of each data file plotted against the file timestamp.

Since these data files are a contiguous list of photon energies and arrival times, the size of each file can be used as a proxy for the total number of photons collected per second, providing a pseudo-lightcurve of the observation. Noticeably, the increased count rates at the beginning and the end of the observation ($t < 170$ s, $t > 980$ s) are associated with an expanded electron belt due to the solar flare at 2025-04-01 $\sim 15:00$ UTC, just prior to the observation.

Using this pseudo-lightcurve, any data files exhibiting an excessive count rate (notably while *SpIRIT* was in the trailing edges of the electron belts, and additionally any temporary spikes) were excluded from the dataset. This threshold was arbitrarily set at 3 kB in size to manage UHF donwlink limitations (with a few exceptions within the first ~ 400 seconds of the observation which were retrieved during earlier downlink attempts as part of a diagnostic process). The included/downlinked files are shown in orange in Figure 3. This process resulted in a list of 730 files, equivalent to 730 non-contiguous seconds of observational data of the Crab Pulsar/Nebula. Given that the files all originate from a single uninterrupted *HERMES* operation, the internal instrument atomic clock ensures the photon events in the dataset have high-precision relative timing to the nominal sub-microsecond precision.

Datasets from observations conducted prior to 2025-04-01 have individual exposure times shorter than 400 s and are therefore not sufficient, when considered individually, to yield a statistically significant pulse profile, as discussed below. Moreover, these are not considered here given that the absolute timing is not available for combination across power cycling of the HERMES instrument in absence of the actual GPS signal for clock synchronization.

3. CRAB ABSOLUTE TIMING

The Crab pulsar Pulse Profile is folded into $n_{\text{bins}} = 15$ phase channels using the effective *SpIRIT* exposure of $T_{\text{exp}} = 730$ s performed on 2025-04-01 at 15:36:06 UTC described above. Event energies are reconstructed with the

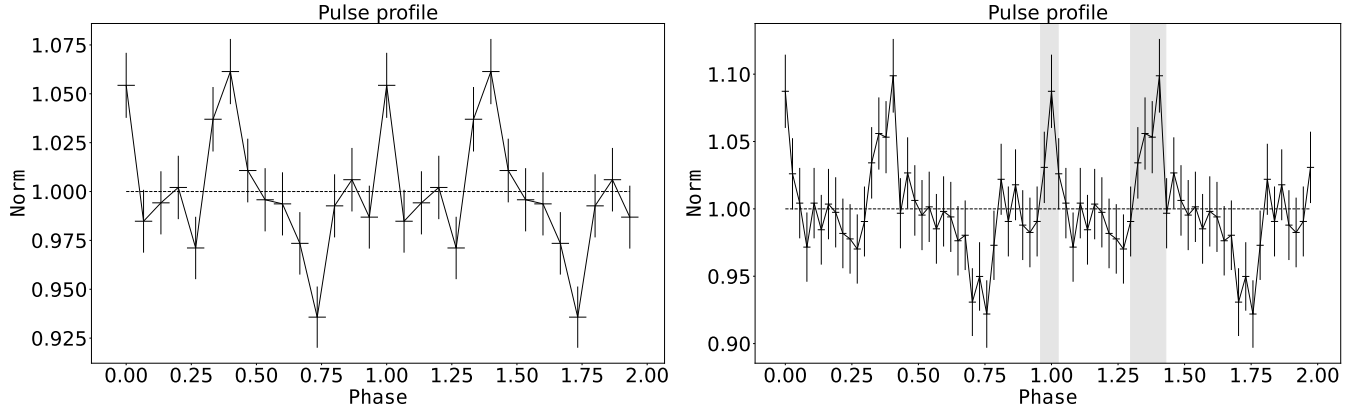


Figure 4. *SpIRIT/HERMES* CRAB pulse profiles in the 3–11.5 keV band; barycentric-corrected times of arrival are folded with $P \simeq 33.84$ ms. **Left:** 15-channel profile with $\sim 5\sigma$ significance. **Right:** 37-channel profile with $\sim 4\sigma$ significance. The gray-shaded region indicates the peak locations and widths as inferred from the profile in Appendix C.

standard gain/offset calibration by using the HERMESDAS reduction pipeline (S. Puccetti et al. 2024). We retain photons in the 3–22 keV X-mode band. We note that an X-mode detection does not automatically translate into an S-mode detection. For a Crab-like spectrum, the S-mode statistics in the ~ 30 keV–2 MeV range do not allow a significant pulsed profile determination within a single $\lesssim 10^3$ s exposure. While observation stacking would be required, the current *SpIRIT/HERMES* configuration does not ensure phase connection across segments, preventing a reliable multi-segment S-mode detection.

3.1. Barycentric Correction and Ephemeris Folding

Pulse phases were computed by correcting the photon times of arrival with respect to the ephemeris reported in the Jodrell Bank (JB) monthly Crab database³ after extrapolating the database solution closest to the observation epoch (2025-03-17, MJD 60751). Other solutions for previous or subsequent epochs were also tested, yielding results similar to those obtained with the original solution.

The spacecraft trajectory was reconstructed by propagating the closest-in-time two-line-element (TLE) orbital ephemeris⁴ set with the SGP4 algorithm (D. Vallado et al. 2006). Photon arrival times were subsequently converted to the Solar System barycenter with the HEASOFT task `barycorr`, adopting the pulsar International Celestial Reference System (ICRS) coordinates and the propagated spacecraft ephemeris.

The Crab pulsar coordinates were taken from the Gaia DR3 catalog⁵ (Gaia Collaboration et al. 2023). The Gaia DR3 coordinates were propagated from the reference epoch J2016.0 to the observation date by applying the proper motions in right ascension and declination as:

$$\begin{aligned}\alpha(t) &= \alpha_0 + \mu_{\alpha^*} (t - t_0), \\ \delta(t) &= \delta_0 + \mu_{\delta} (t - t_0)\end{aligned}\tag{1}$$

where μ_{α^*} and μ_{δ} are expressed in mas yr^{-1} and reported in the Gaia DR3 catalog.

Starting from the JB solution for the P_0 and \dot{P} quoted in the catalog at $t_0 = \text{MJD } 60751$, we propagate the spin period to the epoch of the *SpIRIT* observation t :

$$P(t) = P_0 + \dot{P} (t - t_0).\tag{2}$$

Hereafter, we adopt the resulting period as the HEASOFT `efold`⁶ folding period of the barycentric-corrected time-of-arrivals.

³ see, <https://www.jb.man.ac.uk/pulsar/crab/all.gro>

⁴ see, Space-Track TLE archive for *SpIRIT* on 04-01-2025.

⁵ see, <https://gea.esac.esa.int/archive/>, source_id=3403818172572314624

⁶ <https://heasarc.gsfc.nasa.gov/docs/software/xronos/examples/efold.html>

3.2. Energy resolved profile

We select data across several energy bands to assess the impact of noise on signal significance, while keeping the folding parameters constant.

Consistent with the Crab pulsar spectral energy distribution peaking at 3–5 keV (S. Brandt et al. 2003), we found that the pulse-profile significance is maximized when a low-energy cut is set to 3 keV. As previously discussed, although the instrument’s effective area decreases between 3 and 5 keV and the nominal hardware threshold is ~ 5 keV, channel-to-channel non-uniform response yields a spread in the *effective* thresholds, leaving non-negligible acceptance down to ~ 3 keV.

The profile significance is evaluated by testing the null hypotheses that a flat signal is in our data (i.e., the mean of the profile) and evaluating the χ^2 :

$$\chi^2 = \sum_{i=1}^N \frac{(I_i - \langle I \rangle)^2}{\sigma_i^2}, \quad (3)$$

where I_i is the intensity of the profile and σ_i the associated uncertainties.

The 3–11.5 keV energy range was identified as the one showing the most significant pulse profile; the obtained profile with 15 folding channels is shown in Figure 4, and the significance is $\sim 5\sigma$ (i.e., $\chi^2 = 57.5$ with dof = 14). This is in agreement with the distribution of the expected χ^2 value from the Monte Carlo simulations in subsection A.2. The pulsation significance evaluated over the full X-mode band (3–20 keV) is $\sim 4\sigma$ (i.e., $\chi^2 = 44$ for dof = 14). This reduced significance is driven by the lower Crab Pulsar statistics of the higher energy emission (>10 keV) and by the increasingly background-dominated count rate, with a substantial contribution from the cosmic X-ray background and from the Crab Nebula emission (D. E. Gruber et al. 1999; M. G. Kirsch et al. 2005).

The phase separation between the two peaks is compatible with the typical Crab profile ($\Delta\phi \approx 0.4$). In particular, the peak widths and phase positions in the 37-bin *HERMES* profile (Figure 4) agree with those of the schematic RXTE template shown in Appendix C.

Given the uncertainty in the mock GPS time reference, the absolute phase cannot be constrained. Consistently, when applying several phase shift to the pulse profile in Figure 4, the χ^2 varies with only within the expected statistical scatter (i.e., $\sigma_{\chi^2} = \sqrt{2 \text{dof}}$). For completeness, the maximum χ^2 occurs for an initial phase offset of $\frac{6}{15}$ of the period.

These results are nevertheless consistent with an uncertainty in the absolute phase arising from time-tagging inaccuracies, themselves a consequence of the absence of on-board GPS time discipline, given that an offset of ± 2.0 s is estimated to be present in the photon timestamps during the observation due to the initialisation of the *HERMES* atomic clock with a mock GPS signal based on the main spacecraft computer clock. However, the injection of systematic shifts in the orbital file, within the range of ± 60 s (i.e., corresponding to a positional uncertainty of ± 500 km, which greatly exceeds the expected uncertainty), shows no impact on the pulse profile shape or significance, apart from a shift in the absolute folding phase. However, we note that while the analysis is robust against absolute shift of timestamp offsets, the absolute timing-offset uncertainties do not allow us to determine the absolute pulsar phase for the *SpIRIT* observation, as reported in the JB catalog.

3.3. Period blind search

An independent analysis of this Crab observation was done using the SKYFIELD and ASTROPY libraries in Python for TLE propagation and barycentric correction. The phase ϕ of each photon was calculated as

$$\phi = \text{mod}\left(\phi_0 + \nu t + \frac{1}{2}\dot{\nu}t^2\right), \quad (4)$$

where the frequency ν and its derivative $\dot{\nu}$ were taken from the JB database as previously discussed. We found the highest two-peak significance at $\phi_0 = 0.4$, consistent with the previous *barycorr*-based analysis to within half a phase-bin width ($1/(2 \times 15) \approx 0.033$). The obtained pulse profile was consistent with the one shown in Figure 4. From the barycentric-corrected photon arrival times (Skyfield–Astropy correction), we computed a Lomb–Scargle (LS) periodogram (N. R. Lomb 1976; J. D. Scargle 1982), assigning unit weights to each event. This unbinned approach is computationally efficient and its power normalization is independent of the source flux. We scanned all the periods in the 33–34 ms window, with a 1 μ s step. The statistical significance of the LS peaks was estimated via Monte Carlo simulations with 10^5 realizations. Our analysis revealed six formally significant peaks ($> 3\sigma$), with the highest

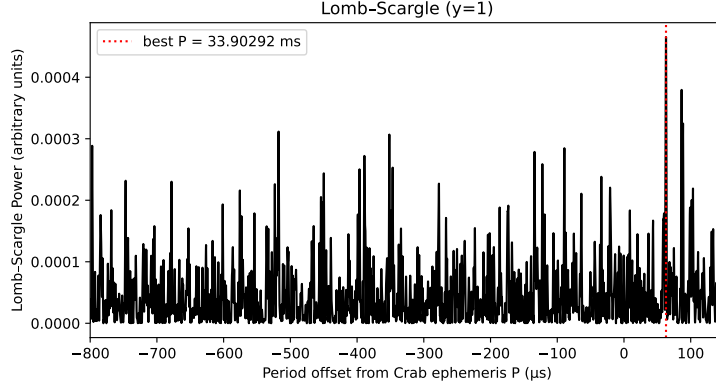


Figure 5. Blind period search with a Lomb–Scargle periodogram in the 33–34 ms range: the highest peak selects the candidate period $P = 33.9$ ms.

one ($> 3.6\sigma$) matching the Crab period, at $P_{\text{LS}} = 33.9$ ms. A conditioned Monte Carlo test, fixing the Crab peak and randomizing the remaining phases within the GTIs, shows that the other peaks are consistent with GTI-window sidelobes, reducing their effective significance to $< 1\sigma$. The P_{LS} and its uncertainty were also validated via a bootstrap resampling, leading to $\sigma_{\text{LS,bs}} = 30 \mu\text{s}$. With this uncertainty, P_{LS} is consistent with the ephemeris period expected at the epoch of the *SpIRIT* observation, $P(t)$, within $2\sigma_{\text{LS,bs}}$.

4. INSTRUMENTS COMPARISON

As a further check of the derived *SpIRIT/HERMES* pulse profile, we use *NICER* and *NuSTAR* data to benchmark the timing performance of *SpIRIT* against both instruments and to validate the recovered pulse profile by adopting the *NICER/NuSTAR* profiles as reference templates. The barycentric correction and folding are applied for the observation epochs as treated in the previous section. Moreover, we used the *RXTE* Crab pulse profile as a reference template to assess the significance of the pulse profile measured by *SpIRIT*.

4.1. *NuSTAR* and *NICER* data extraction

We extract data from the closest *NuSTAR* observation to the *SpIRIT* Crab Pulsar observation, which started on 2025-04-05 at 22:32:21.9340 UTC with an exposure of $T_{\text{exp}} = 14.7$ ks. Data were retrieved from the *NuSTAR* target search website⁷. We considered filtered data and orbital file as provided by the archive and applied the *NuSTAR* CALDB clock correction to the event list.

We also retrieved *NICER* data from the *NICER* archive⁸. We consider the latest available *NICER* observation of the Crab pulsar, taken on 2025-02-28 18:55:18.00, with 1.4 ks exposure time, and downloaded cleaned data with the associated orbital file.

4.2. *SpIRIT* profile modeling

We derive the *NuSTAR* pulse profile I_{Nu} by considering the same number of channels as the *SpIRIT* profile in Figure 4. We analyze the *SpIRIT* profile by fitting it with the model profile:

$$I_{\text{mp}} = A \times I_{\text{Nu}}(x + \phi) + C, \quad (5)$$

where A is the scale factor of the model and C is an additive constant. The two profiles are not in phase, so we consider a free parameter ϕ to apply a shift to the model in order to minimize the χ^2 that depends on the grade of similarity between the *NuSTAR* profile and the *SpIRIT* one. I_{mp} is the intensity of the model profile derived from the *NuSTAR* profile I_{Nu} . We fit the *SpIRIT* profile by minimizing χ^2 with respect to A , C , and the phase shift ϕ , with $\phi \in [0, 1)$. The best-fit phase shift is $\phi = 0.667$, while the best-fit parameters are $A = 0.41 \pm 0.073$ and $C = 0.59 \pm 0.072$.

Considering the uncertainties associated with the *SpIRIT* observation and the best-fit parameters (A, C, ϕ), Figure 6 shows the reliability of the pulse profile. The reduced chi-square is $\chi^2_{\nu} = 1.33$ with $\nu = 15 - 2 = 13$ degrees of freedom

⁷ https://heasarc.gsfc.nasa.gov/db-perl/NuSTAR_table

⁸ https://heasarc.gsfc.nasa.gov/db-perl/NICER_table

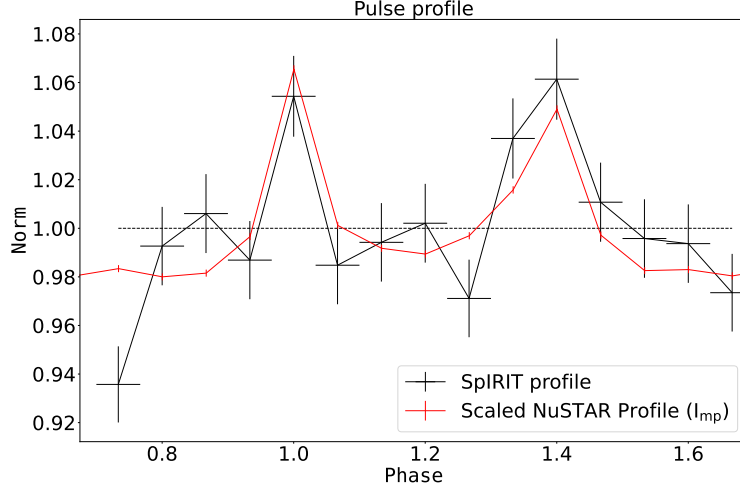


Figure 6. The Crab Pulse profile measured by *SpIRIT* (15 phase bins, 3–11.5 keV band) is fitted with the NuSTAR model in Equation 5. The solid red curve shows the NuSTAR modulated profile (15 phase bins, 3–11.5 keV band) for the best-fit parameters A , C , and ϕ .

(i.e., $\chi^2 = 17.29$). Thus, the data are statistically consistent with the model, and there is no evidence to reject the fit at conventional significance levels.

4.3. Epoch folding search

Further proof of the profile accuracy is obtained by performing an epoch-folding search (`efsearch`) around the JB catalogue-expected Crab Pulsar ephemeris, as in Equation 2, with a 100 ns resolution. This value is the accuracy of the on-board time-stamping and therefore limits the precision of the best-period search. The `efsearch` best period is $P_{\text{best}} = 33.8394$ ms, which is $0.5 \mu\text{s}$ smaller with respect to the period derived from the radio ephemeris.

The expected period is highlighted in Figure 7, whose difference from the best `efsearch` period is perfectly compatible with the first-order error on the period determination ΔP , defined as:

$$\Delta P = \frac{P^2}{T_{\text{exp}}} \approx 1.5 \mu\text{s}, \quad (6)$$

where T_{exp} is the observation exposure time, $T_{\text{exp}} = 730$ s. However, the Gaussian fit to the narrow `efsearch` peak shows that the *SpIRIT* best-fit period is consistent with the JB ephemeris at the observation epoch within $\sim 2.5\sigma$, where σ is the standard deviation of the *SpIRIT/HERMES* Gaussian profile shown in Figure 7.

To compare the timing capabilities of *SpIRIT* with *NuSTAR* and *NICER*, we applied `efsearch` to *NuSTAR* and *NICER* data in the same energy band considered for the `efsearch` in Figure 7. We restrict the exposure so that the resulting detection significance matches that obtained with *SpIRIT* (see Figure 7) and take into account the same Crab ephemerids used for the *SpIRIT* data.

We therefore decrease the exposure time for *NuSTAR* and *NICER* data. Due to that, the `efsearch` step is:

$$t_{\text{step}} = \frac{P^2}{T_{\text{exp}} n_{\text{bins}}}, \quad (7)$$

which sets the period resolution shown in Figure 7. As expected, thanks to the larger effective area of the two instruments, they require a smaller exposure time to reach the *HERMES* detection significance (*NuSTAR* ≈ 95 s of exposure time, while for *NICER* ≈ 9 s).

4.4. SpIRIT profile validation

To validate the correct operation of the *SpIRIT/HERMES* payload and the observed pulse profile, we compare the measured significance with the predictions from the analytical and Monte Carlo analyses in subsection A.2. We normalize an RXTE Crab Pulsar pulse-profile to the count rate (i.e., counts s^{-1}) of the *HERMES* payload by considering the Cosmic X-ray Background (CXB) background and the Nebula/Pulsar contributions. First, we analytically

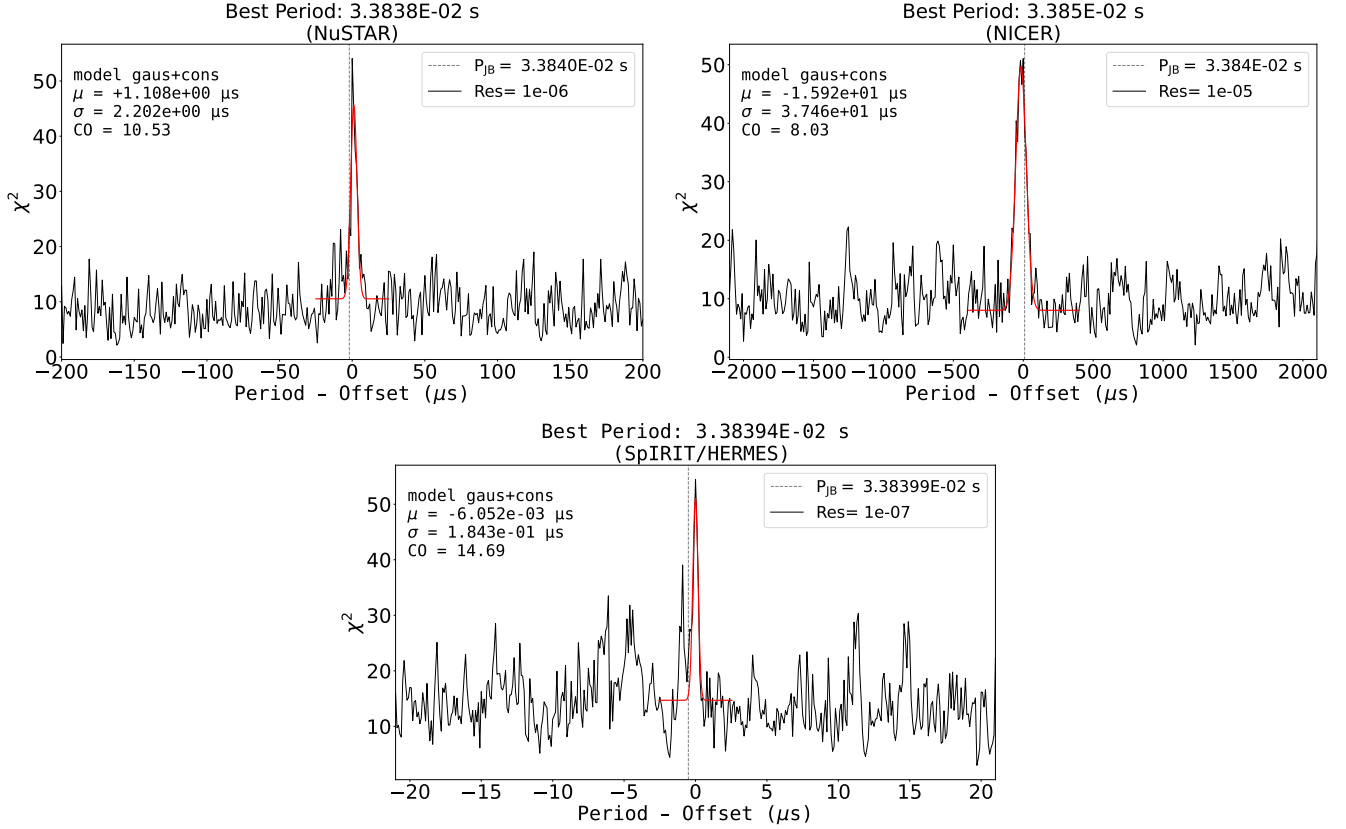


Figure 7. Epoch folding search around the expected JB catalog period at different search grid resolution, which depends on the considered exposure time. We used $n_{\text{bins}} = 15$ for the 3–11.5 keV energy band and P, \hat{P} relative to the observing epoch. Panels show the Gaussian fit of the `efsearch` for each considered instrument.

estimate the exposure time required to guarantee a significance of at least $\gtrsim 3\sigma$ (see Appendix B). This analysis confirms that the observed 730 s exposure is sufficient to exceed this threshold.

We then evaluate the statistical power of the detection for the fixed 730 s exposure, via Monte Carlo simulations. We generated synthetic realizations of the *HERMES* pulse profile according to the Poissonian statistic, and computed the χ^2 against the mean count rate for each instance. We consider as lower threshold the χ^2 associated to a 3σ detection for 15 bins (i.e., $\chi_{\text{th},3\sigma}^2 = 35.25$). The results indicate that the probability of obtaining a χ^2 value exceeding the $\chi_{\text{th},3\sigma}^2$ is $P(\chi^2 > \chi_{\text{th},3\sigma}^2) \simeq 82\%$. This confirms that the significance measured for the reported Crab profile is fully consistent with the expected non-central χ^2 distribution in see subsection A.2.

The consistency between the analytical/MonteCarlo predictions and the observed data validates the instrument performance, indicating that the results are governed by Poisson statistics.

5. DISCUSSION AND CONCLUSION

We performed millisecond X-ray timing with an on-axis dataset of $T_{\text{exp}} = 730 \text{ s}$ from a single 1200 s operation, obtained by the wide field of view *HERMES* payload onboard the 6U $\sim 11 \text{ kg}$ nanosatellite *SpIRIT*. By folding photon time of arrivals at the JB ephemeris, extrapolated to the observation epoch, we resolved the canonical Crab pulsar double-peaked pulse profile with a statistical significance of 5.0σ in the 3–11.5 keV band. The *SpIRIT/HERMES* pulse shape was validated through a template fit to the closest-in-time NuSTAR observation of the Crab pulsar. Moreover, an epoch-folding search on the *SpIRIT* data, recovered a best period of 33.839 ms, only $0.5 \mu\text{s}$ shorter than the expected value of the catalog and entirely consistent with the Fourier resolution limit of $\Delta P \sim 1.5 \mu\text{s}$ achievable with the available *SpIRIT/HERMES* exposure time.

These results demonstrate that the instrument atomic clock, the SGP4 orbit propagation, and the `barycorr` correction, preserve the phase coherence to within a few microseconds over the 20-minute observation window.

In addition, to confirm the validity of the *SpIRIT* pulse profile significance, we carried out an analytical treatment and Monte Carlo simulations using the *RXTE* Crab pulse profile as a theoretical template. This allowed us to predict the expected significance by taking into account the exposure time and the characteristics of the *HERMES* payload (e.g., instrument effective area, pointing, response matrix) for the Crab observation. Since the computed significance is in full agreement with these predictions, we can confirm that the instrument is operating correctly and that the measurement process is governed by the expected Poisson statistics.

Our conclusion is that high-precision timing, once restricted to large, resource-intensive observatories, can be achieved with cost-effective CubeSats. Reaching a $\gtrsim 5\sigma$ detection of a short-period pulsar in just 12 minutes of exposure, with a $\lesssim 50\text{cm}^2$ instrument effective area, highlights both the effectiveness of the highly compact *HERMES* payload and the potential of low-cost, fast-development nanosatellite missions for high-energy astrophysics.

ACKNOWLEDGMENTS

This work was supported by the Horizon 2020 programme (AHEAD2020, Grant Agreement No. 871158; HERMES-SP, Grant Agreement No. 821896), and from ASI-INAF agreements for the HERMES Technological Pathfinder (HTP; scientific activities) and HERMES Pathfinder (operations and scientific exploitation). The *SpIRIT* mission is led by the University of Melbourne (PI Michele Trenti), which received funding through the International Space Investment - Expand Capability grant funding scheme managed by the ASA for mission development and launch, and through the Moon to Mars - Mission Demonstrator scheme of ASA for mission operations. WL acknowledges doctoral funding from the Space Science and Technology PhD programme (University of Trento, Cycle XXXVIII). MD acknowledges support from the Czech Science Foundation (GAČR), project No. 24-11487J.

REFERENCES

- Baroni, G., Campana, R., Evangelista, Y., et al. 2024, in Society of Photo-Optical Instrumentation Engineers (SPIE) Conference Series, Vol. 13093, Space Telescopes and Instrumentation 2024: Ultraviolet to Gamma Ray, ed. J.-W. A. den Herder, S. Nikzad, & K. Nakazawa, 130935O, doi: [10.1117/12.3018308](https://doi.org/10.1117/12.3018308)
- Brandt, S., Budtz-Jørgensen, C., Lund, N., et al. 2003, A&A, 411, L243, doi: [10.1051/0004-6361:20031363](https://doi.org/10.1051/0004-6361:20031363)
- Campana, R., Fuschino, F., Evangelista, Y., Dilillo, G., & Fiore, F. 2020, in Space Telescopes and Instrumentation 2020: Ultraviolet to Gamma Ray, ed. J.-W. A. den Herder, K. Nakazawa, & S. Nikzad (SPIE), doi: [10.1117/12.2560365](https://doi.org/10.1117/12.2560365)
- Campana, R., Baroni, G., Della Casa, G., et al. 2022, in Space Telescopes and Instrumentation 2022: Ultraviolet to Gamma Ray, ed. J.-W. A. den Herder, K. Nakazawa, & S. Nikzad (SPIE), 249, doi: [10.1117/12.2629031](https://doi.org/10.1117/12.2629031)
- Campana, R., Evangelista, Y., Fiore, F., et al. 2024, in Space Telescopes and Instrumentation 2024: Ultraviolet to Gamma Ray, ed. J.-W. A. den Herder, K. Nakazawa, & S. Nikzad (SPIE), 245, doi: [10.1117/12.3018007](https://doi.org/10.1117/12.3018007)
- del Castillo, M. O., McRobbie, J., Woods, A., et al. 2025, Acta Astronautica, 236, 359, doi: <https://doi.org/10.1016/j.actaastro.2025.06.050>
- Dilillo, G., Marchesini, E., Della Casa, G., et al. 2024, Astronomy and Computing, 46, 100797, doi: [10.1016/j.ascom.2024.100797](https://doi.org/10.1016/j.ascom.2024.100797)
- Evangelista, Y., Fiore, F., Fuschino, F., et al. 2020a, in Space Telescopes and Instrumentation 2020: Ultraviolet to Gamma Ray, ed. J.-W. A. den Herder, K. Nakazawa, & S. Nikzad (SPIE), doi: [10.1117/12.2561018](https://doi.org/10.1117/12.2561018)
- Evangelista, Y., Fiore, F., Fuschino, F., et al. 2020b, in Space Telescopes and Instrumentation 2020: Ultraviolet to Gamma Ray, ed. J.-W. A. den Herder, K. Nakazawa, & S. Nikzad (SPIE), doi: [10.1117/12.2561018](https://doi.org/10.1117/12.2561018)
- Evangelista, Y., Fiore, F., Campana, R., et al. 2024, in Space Telescopes and Instrumentation 2024: Ultraviolet to Gamma Ray, ed. J.-W. A. den Herder, K. Nakazawa, & S. Nikzad (SPIE), 74, doi: [10.1117/12.3018259](https://doi.org/10.1117/12.3018259)
- Fiore, F., Werner, N., & Behar, E. 2021, Distributed Architectures and Constellations for Gamma-Ray Burst Science, <https://arxiv.org/abs/2112.08982>
- Fiore, F., Burderi, L., Lavagna, M., et al. 2020, in Space Telescopes and Instrumentation 2020: Ultraviolet to Gamma Ray, ed. J.-W. A. den Herder, K. Nakazawa, & S. Nikzad (SPIE), doi: [10.1117/12.2560680](https://doi.org/10.1117/12.2560680)
- Fiore, F., Trenti, M., Evangelista, Y., et al. 2025, HERMES Pathfinder & SpIRIT: a progress report, <https://arxiv.org/abs/2502.17952>

- Gaia Collaboration, Vallenari, A., Brown, A. G. A., et al. 2023, *A&A*, 674, A1, doi: [10.1051/0004-6361/202243940](https://doi.org/10.1051/0004-6361/202243940)
- Gandola, M., Mele, F., Grassi, M., Malcovati, P., & Bertuccio, G. 2021, *Journal of Instrumentation*, 16, T12013, doi: [10.1088/1748-0221/16/12/T12013](https://doi.org/10.1088/1748-0221/16/12/T12013)
- Ghirlanda, G., Nava, L., Salafia, O., et al. 2024, *Astronomy & Astrophysics*, 689, A175, doi: [10.1051/0004-6361/202450006](https://doi.org/10.1051/0004-6361/202450006)
- Gruber, D. E., Matteson, J. L., Peterson, L. E., & Jung, G. V. 1999, *ApJ*, 520, 124, doi: [10.1086/307450](https://doi.org/10.1086/307450)
- Hurley, K., Pal'shin, V. D., Aptekar, R. L., et al. 2013, *ApJS*, 207, 39, doi: [10.1088/0067-0049/207/2/39](https://doi.org/10.1088/0067-0049/207/2/39)
- Jain, C., & Paul, B. 2011, *Research in Astronomy and Astrophysics*, 11, 1134–1142, doi: [10.1088/1674-4527/11/10/002](https://doi.org/10.1088/1674-4527/11/10/002)
- Kirsch, M. G., Briel, U. G., Burrows, D., et al. 2005, in *UV, X-Ray, and Gamma-Ray Space Instrumentation for Astronomy XIV*, ed. O. H. W. Siegmund (SPIE), doi: [10.1117/12.616893](https://doi.org/10.1117/12.616893)
- Leone, W., Burderi, L., Di Salvo, T., et al. 2025, *Astronomy & Astrophysics*, 701, A50, doi: [10.1051/0004-6361/202453054](https://doi.org/10.1051/0004-6361/202453054)
- Lomb, N. R. 1976, *Ap&SS*, 39, 447, doi: [10.1007/BF00648343](https://doi.org/10.1007/BF00648343)
- Madsen, K. K., Harrison, F. A., Markwardt, C. B., et al. 2015, *ApJS*, 220, 8, doi: [10.1088/0067-0049/220/1/8](https://doi.org/10.1088/0067-0049/220/1/8)
- Mearns, R., Chapman, A., & Trenti, M. 2024, arXiv e-prints, arXiv:2407.19623, doi: [10.48550/arXiv.2407.19623](https://doi.org/10.48550/arXiv.2407.19623)
- Ortiz del Castillo, M., Therakam, C., McRobbie, J., et al. 2024a, arXiv e-prints, arXiv:2407.14031, doi: [10.48550/arXiv.2407.14031](https://doi.org/10.48550/arXiv.2407.14031)
- Ortiz del Castillo, M., Morgan, J., McRobbie, J., et al. 2024b, arXiv e-prints, arXiv:2404.08399, doi: [10.48550/arXiv.2404.08399](https://doi.org/10.48550/arXiv.2404.08399)
- Puccetti, S., Perri, M., Campana, R., et al. 2024, in *Society of Photo-Optical Instrumentation Engineers (SPIE) Conference Series*, Vol. 13098, *Observatory Operations: Strategies, Processes, and Systems X*, ed. C. R. Benn, A. Chrysostomou, & L. J. Storrie-Lombardi, 130980O, doi: [10.1117/12.3018828](https://doi.org/10.1117/12.3018828)
- Pál, A., Ohno, M., Mészáros, L., et al. 2023, GRBAlpha: the smallest astrophysical space observatory – Part 1: Detector design, system description and satellite operations, <https://arxiv.org/abs/2302.10048>
- Rots, A. H., Jahoda, K., & Lyne, A. G. 2004, *The Astrophysical Journal*, 605, L129–L132, doi: [10.1086/420842](https://doi.org/10.1086/420842)
- Scargle, J. D. 1982, *ApJ*, 263, 835, doi: [10.1086/160554](https://doi.org/10.1086/160554)
- Swank, J. H. 1999, *Nuclear Physics B Proceedings Supplements*, 69, 12, doi: [10.1016/S0920-5632\(98\)00175-3](https://doi.org/10.1016/S0920-5632(98)00175-3)
- Tamagawa, T., Enoto, T., Kitaguchi, T., et al. 2025, *Publications of the Astronomical Society of Japan*, 77, 466–479, doi: [10.1093/pasj/psaf014](https://doi.org/10.1093/pasj/psaf014)
- Thomas, M., Trenti, M., Sanna, A., et al. 2023, *Publications of the Astronomical Society of Australia*, 40, doi: [10.1017/pasa.2023.4](https://doi.org/10.1017/pasa.2023.4)
- Trenti, M., del Castillo, M. O., Mearns, R., et al. 2024, *SpIRIT Mission: In-Orbit Results and Technology Demonstrations*, <https://arxiv.org/abs/2407.14034>
- Vallado, D., Crawford, P., Hujsak, R., & Kelso, T. 2006, *Revisiting Spacetrack Report #3 (AIAA)*, 1–94, doi: [10.2514/6.2006-6753](https://doi.org/10.2514/6.2006-6753)
- van der Klis, M. 2006, in *Compact stellar X-ray sources*, ed. W. H. G. Lewin & M. van der Klis, Vol. 39, 39–112
- Vivekanand, M. 2021, *Astronomy & Astrophysics*, 649, A140, doi: [10.1051/0004-6361/202140358](https://doi.org/10.1051/0004-6361/202140358)
- Weisskopf, M. C., Tennant, A. F., Yakovlev, D. G., et al. 2011, *The Astrophysical Journal*, 743, 139, doi: [10.1088/0004-637x/743/2/139](https://doi.org/10.1088/0004-637x/743/2/139)

APPENDIX

A. CRAB PULSAR EXPOSURE WITH HERMES: ANALYTICAL ESTIMATE WITH MC VALIDATION

In general, determining the exposure time required to detect a neutron star pulsed profile is not straightforward. The calculations presented in this appendix show, both analytically and through simulations, how to assess an $n\sigma$ -level detection as a function of a given exposure time, T_{exp} .

We adopt as a template the folded *Rossi X-ray Timing Explorer* (RXTE, J. H. Swank 1999) pulse profile of the Crab pulsar reported by C. Jain & B. Paul (2011). Assuming an on-axis pointing, we compute the exposure time required for the two peaks to reach the desired statistical significance.

By considering the detector response files, we simulated the count spectrum expected for *HERMES* with the `fakeit` task in XSPEC, modeling it as the superposition of three components: (i) the Crab Nebula, whose spectral parameters were taken from M. G. Kirsch et al. (2005); (ii) the pulsed emission of the Crab pulsar, described by the model in M. C. Weisskopf et al. (2011); and (iii) the diffuse X-ray background.

The CXB is derived from the diffused CXB model proposed in D. E. Gruber et al. (1999). We assume a low energy *HERMES/SpIRIT* FoV of 1.57 steradians as in G. Ghirlanda et al. (2024), for the 3–11.5 keV energy band.

In the current configuration of the *HERMES* instrument onboard *SpIRIT*, the nominal energy lower cut threshold is set at a level equivalent to about 5 keV. However, the precise energy threshold for each active channel may vary due to channel-to-channel process variations and the discrimination circuit’s working principle Y. Evangelista et al. (2020b). This leads to a significant threshold spread, and a particular sensitivity also in the 3–5 keV band. Accordingly, throughout we adopted a lower-energy cut of 3 keV.

An appropriate set of *HERMES* Ancillary Response Files (*arf*) and Redistribution Matrix Files (*rmf*) (R. Campana et al. 2020) has been built to take this effect into account, and was used to evaluate the average count rate in the 3–11.5 keV energy range for the Crab Nebula+Pulsar (C_{Crab}) and the CXB (C_{BKG}).

A.1. Analytical determination of the Crab exposure time

The dominant practical limitation is the on-axis exposure that can accumulate over time. In this section, we present the analytical treatment for deriving a relation linking the expected χ^2 of the Crab pulse profile to the observing time T_{exp} .

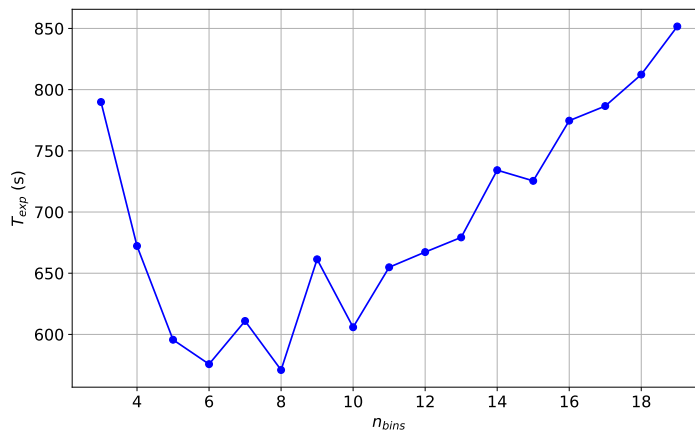


Figure 8. Required exposure time to obtain a χ^2 threshold for a 3σ level detection as function of n_{bins} . Although analytically derived, the observed scatter in Figure 8 arises because the solution is applied to an observed profile with finite counts and is therefore subject to statistical (Poisson) fluctuations.

Appendix B shows the analytical solution to the problem, and by solving the Equation B9 for T_{exp} , we find that the χ^2 value can be expressed as:

$$\chi_{\text{th}}^2 = T_{\text{exp}} \cdot C_{\text{Crab}} \cdot \sum_{i=1}^{n_{\text{bins}}} \frac{(\text{FRAC}_i - \Delta\phi)^2}{\text{FRAC}_i + \Delta\phi \cdot \left(\frac{C_{\text{BKG}}}{C_{\text{Crab}}}\right)}, \quad (\text{A1})$$

where FRAC_i is the per-bin pulsed fraction that maximizes the pulse significance, as defined in [Appendix C](#) and [Equation C10](#) and $\Delta\phi$ the dimension of the phase bin.

We now assume, as null hypotheses, a flat signal in our data (H_0 corresponds to no Crab pulsation detection). The probability that, for a given threshold $\chi_{\text{th,dof}}^2$, the observed χ^2 is greater, comes from a well-known function $P(\chi^2 \geq \chi_{\text{th,dof}}^2)$, for a certain number of degrees of freedom dof.

[Equation A1](#) can be inverted to derive the T_{exp} necessary to get the desired $\chi_{\text{th,dof}}^2$ for a given number of degrees of freedom n_{bins} . We compute the $\chi_{\text{th,dof}}^2$ to reach a 3σ significance level for each bin, and obtain the trend shown in [Figure 8](#).

A.2. The Monte Carlo validation

The previous discussion is associated with the χ^2 threshold and so with the probability $P(\chi^2 \geq \chi_{\text{th,dof}}^2)$. This establishes the required exposure time to reach a minimum significance limit.

In order to verify the accuracy of the previous solution and the expected χ^2 distribution as a function of a given T_{exp} , we perform a simulation-based analysis starting from a theoretical profile with $n_{\text{bins}} = 15$ as shown in [Figure 10](#).

We adopt a fixed pulse shape template and denote its amplitude by I_p (in counts) as the sum of the CRAB and background contributions:

$$I_p = I_{\text{ratio}} \cdot T_{\text{exp}} \cdot C_{\text{Crab}} + \frac{1}{n_{\text{bins}}} \cdot T_{\text{exp}} \cdot C_{\text{BKG}}, \quad (\text{A2})$$

where I_{ratio} is the ratio of the counts in every bin of the RXTE profile over the total counts as shown in [Figure 10](#). When using the [Equation A2](#), we extract the value of I_p with a Poisson distribution, in order to achieve a series of Poisson realization of the Crab pulse profile at a given exposure time.

According to the observation exposure, in [Equation A2](#), we adopt $T_{\text{exp}} = 730$ s and for each Poisson realization we evaluate the χ^2 with respect to the average of the pulse profile.

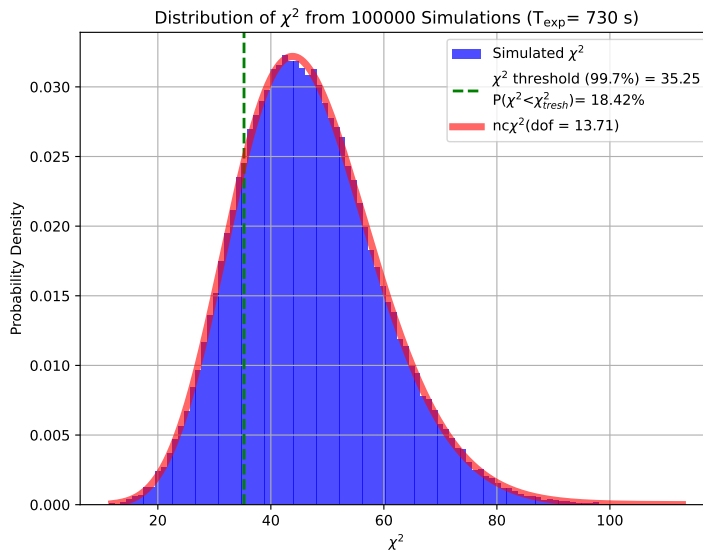


Figure 9. Monte Carlo distribution of the χ^2 statistic for simulated Crab-like pulse profiles with $n_{\text{bins}} = 15$. The histogram is fitted with the probability density in [Equation B3](#). The vertical green line marks the 3σ detection threshold: for dof = 14 we adopt the threshold $\chi^2 = 35.25$, i.e. the 99.7% upper-tail critical value of the central χ^2 distribution.

B. THE ANALYTICAL SOLUTION

The Monte Carlo distribution is shown in [Figure 9](#) is fitted with a non-central χ^2 (nc χ^2) distribution:

$$f(x, dof, \lambda) = \frac{1}{2} \exp\left(-\frac{\lambda + x}{2}\right) \left(\frac{x}{\lambda}\right)^{(dof-2)/4} L_{(dof-2)/2}\left(\sqrt{\lambda x}\right), \quad (\text{B3})$$

where λ is the non-centrality parameter. $L_{(k-2)/2}$ denotes the modified Bessel function of first order of degree and x the χ^2 . The parameters from the nc χ^2 fit match expectations, and the dof are in line with the theoretical value $n_{\text{bins}} - 1 = 15 - 1 = 15$.

Therefore, we expect that in $\approx 81.58\%$ of cases, a 730 s on-axis *HERMES* observation grants at least a 3σ detection.

The total detected count rate (in counts/s) is given by the sum of the Crab emission (nebula + pulsar) C_{Crab} and the background in the *HERMES* FoV C_{BKG} :

$$C_{\text{tot}} = C_{\text{Crab}} + C_{\text{BKG}} \quad (\text{B4})$$

If we divide the pulse profile into n_{bins} bins, as in [Figure 10](#), the total rate in each phase bin ϕ_i is:

$$C_{\text{tot}}(\phi_i) = \Delta\phi \cdot C_{\text{BKG}} + \text{FRAC}_i \cdot C_{\text{CRAB}} \quad (\text{counts/s}), \quad (\text{B5})$$

where $\Delta\phi$ is the bin width and FRAC_i the count ratio evaluated for each bin as in [Figure 10](#).

For an observation time T_{exp} , the expected counts in each phase bin are:

$$N_{\text{tot}}(\phi_i) = C_{\text{tot}}(\phi_i) \cdot T_{\text{exp}}, \quad (\text{B6})$$

with an associated Poissonian error of:

$$\sigma_{N_i} = \sqrt{N_{\text{tot}}(\phi_i)} \quad (\text{B7})$$

The average total value of the expected counts is computed as:

$$\overline{N_{\text{tot}}} = \sum_{i=1}^{n_{\text{bins}}} \frac{N_{\text{tot}}(\phi_i)}{n_{\text{bins}}} \times \Delta\phi, \quad (\text{B8})$$

where $\Delta\phi_{\text{BINS}}$ is the peak dimension in unit of phase. We can now compute the theoretical chi-square value as:

$$\chi_{\text{th}}^2 = \sum_{i=1}^{n_{\text{bins}}} \frac{(N_{\text{tot}}(\phi_i) - \overline{N_{\text{tot}}})^2}{N_{\text{tot}}(\phi_i)}. \quad (\text{B9})$$

C. PULSATION SIGNIFICANCE MAXIMIZATION

To maximize the pulsation significance, we slide the edges of phase bins across the folded profile as in [Figure 10](#).

For every trial position we compute, in each energy channel, the ratio

$$\text{FRAC}_i = \frac{N_i}{N_{\text{on}} + N_{\text{off}}}, \quad i = 1, \dots, n_{\text{bins}}, \quad (\text{C10})$$

i.e. the ratio of counts falling in each bin window N_i to the total counts on-pulse (N_{on}) plus off-pulse (N_{off}), as defined in [Figure 10](#).

The optimal phase shift is found by maximizing the variance

$$\sigma^2 = \frac{1}{n_{\text{bins}}} \sum_{i=1}^{n_{\text{bins}}} (1 - \text{FRAC}_i)^2, \quad (\text{C11})$$

which reaches its maximum when the binning is such that two bins are centered on the main emission peaks of the pulse profile.

Applying this optimization for different numbers of channels, in the 3–11.5 keV energy band, we produce a lookup table that records, the phase boundaries and the corresponding FRAC_i for each profile represented with a given bins number.

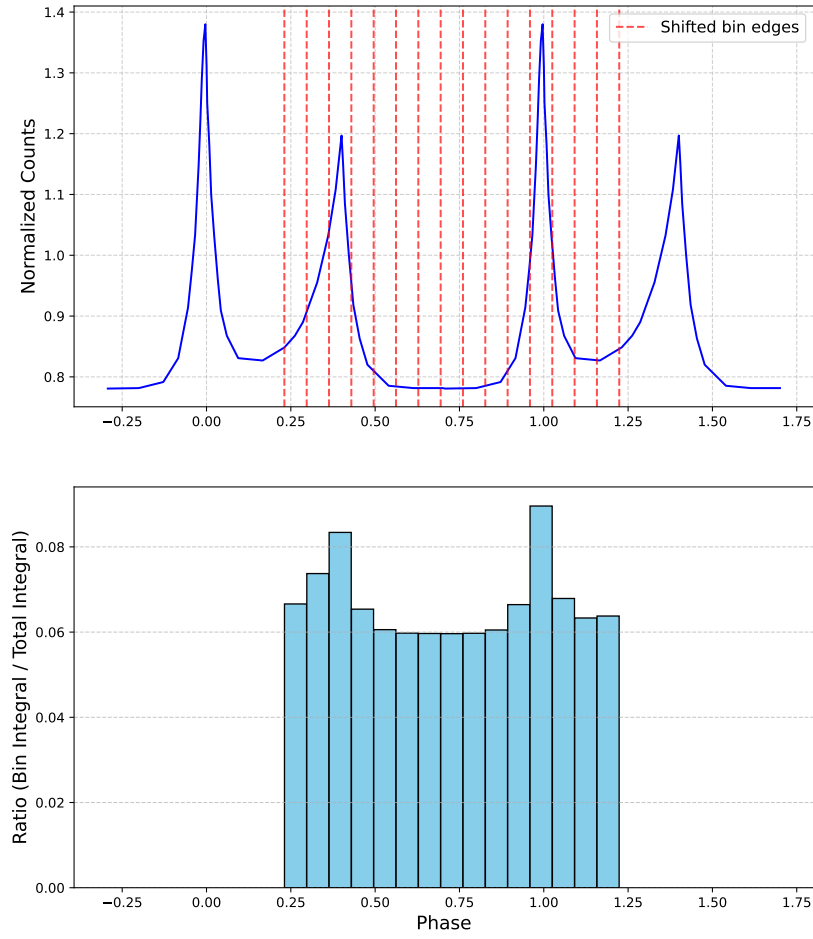


Figure 10. Upper plot: RXTE Crab Pulsar pulse profile is rebinned to obtain a 15-channel profile, for the given best shift. Lower plot: Normalized count ratio as evaluated in the red bins, with respect to total counts of the profile ($FRAC_i$). In this case, the on-pulse peaks are the 3rd and the 12th, the others are considered as off-pulse bins.